

Article

Three-Dimensional Volume Integral Equation Method for Solving Isotropic/Anisotropic Inhomogeneity Problems

Jungki Lee * and Mingu Han

Department of Mechanical and Design Engineering, Hongik University, Sejong City 30016, Korea; h9265@naver.com

* Correspondence: inq3jkl@hongik.ac.kr; Tel.: +82-44-860-2619

Received: 18 September 2020; Accepted: 22 October 2020; Published: 26 October 2020



Abstract: In this paper, the volume integral equation method (VIEM) is introduced for the analysis of an unbounded isotropic solid composed of multiple isotropic/anisotropic inhomogeneities. A comprehensive examination of a three-dimensional elastostatic VIEM is introduced for the analysis of an unbounded isotropic solid composed of isotropic/anisotropic inhomogeneity of arbitrary shape. The authors hope that the volume integral equation method can be used to compute critical values of practical interest in realistic models of composites composed of strong anisotropic and/or heterogeneous inhomogeneities of arbitrary shapes.

Keywords: numerical modelling; multiple isotropic/anisotropic inhomogeneities; three-dimensional volume integral equation method; finite element method; boundary integral equation method; elastostatics/elastodynamics

1. Introduction

The fibers and matrix in composites are usually composed of isotropic material. However, to satisfy advanced composites, a portion of the constituents can be anisotropic. For example, in SiC/Ti (silicon carbide/titanium) metal matrix composites, the matrix is almost isotropic, whereas the SiC fiber has strong anisotropy and consists of an interphase and a core. A transverse cross section of a SiC/Ti-15-3 composite is shown in Figure 1.

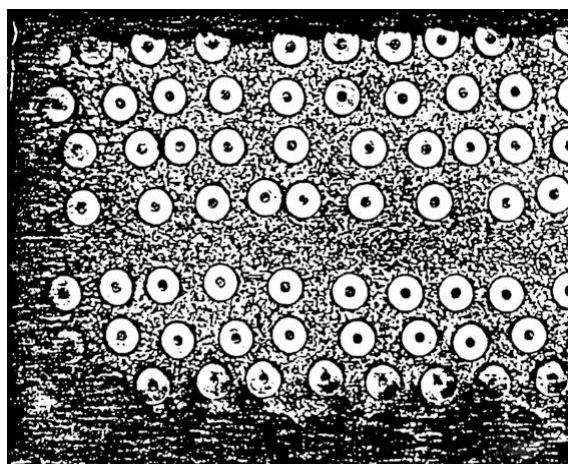


Figure 1. Transverse cross-section of a SiC/Ti-15-3 composite.

Various analytical methods are accessible for solving inhomogeneity problems when the geometry of the inhomogeneities is straightforward (e.g., ellipsoidal, cylindrical and spherical) or when the inhomogeneities are separated well from one another [1–3]. We cannot apply these methods to realistic models for a general problem when the inhomogeneities or voids are of arbitrary shape and the density of the voids or inhomogeneities is high. Therefore, stress analysis of heterogeneous solids frequently requires the utilization of numerical techniques in view of the finite element method (FEM) or the boundary integral equation method (BIEM or BEM). These techniques experience challenges in dealing with problems which include infinite media or multiple anisotropic inhomogeneities. In response to this concern, it has been shown that the volume integral equation method (VIEM) can eliminate both of these limitations in heterogeneous problems which include infinite media [4,5].

By contrast with the BIEM, the VIEM does not require utilization of Green's function for anisotropic inhomogeneities and is not sensitive to the geometry of the inhomogeneities. Moreover, as opposed to the FEM, where the whole domain needs to be discretized, the VIEM needs discretization of the multiple inhomogeneities only.

Problems associated with multiple inhomogeneities have been examined by several authors [6–8]. In this paper, the stress field in an unbounded isotropic elastic matrix, composed of multiple isotropic inhomogeneities and whose number and shape are arbitrary under uniform loading at infinity could be evaluated. The efficiency, accuracy and capability of the volume integral equation method will also be examined using these results.

The VIEM is applied to a class of three-dimensional elastostatic inhomogeneity problems. The details of the numerical treatment, especially the evaluation of singular integrals, for resolving three-dimensional problems in view of the VIEM are introduced in this paper. The accuracy of the VIEM is examined by comparing the results obtained from analytical solutions.

The purpose of this paper is to introduce the volume integral equation method (VIEM) as an efficient numerical method for solving multiple anisotropic inhomogeneity problems.

2. Volume Integral Equation Method (VIEM)

The geometry of the overall elastodynamic problem considered herein is shown in Figure 2a. It is assumed that an unbounded isotropic elastic solid, containing a number of isotropic or anisotropic inhomogeneities of arbitrary shape, is subjected to prescribed dynamic loading at infinity. In Figure 2a, V and S show the volume and surface of the inhomogeneity and the symbol \mathbf{n} indicates the outward unit normal to S . The symbols $\rho^{(1)}$ and $c_{ijkl}^{(1)}$ denote the density and fourth-order elasticity tensors of the inhomogeneity whereas $\rho^{(2)}$ and $c_{ijkl}^{(2)}$ denote the density and the fourth-order elasticity tensors of the unbounded matrix material. The unbounded matrix material is presumed to be isotropic and homogeneous, so that $c_{ijkl}^{(2)}$ is a constant isotropic tensor, whereas $c_{ijkl}^{(1)}$ can be arbitrary. Therefore, the inhomogeneities may, in general, be anisotropic and inhomogeneous. The interfaces between the inhomogeneities as well as the unbounded matrix material are assumed to be perfectly bonded, ensuring continuity of the stress and displacement vectors.

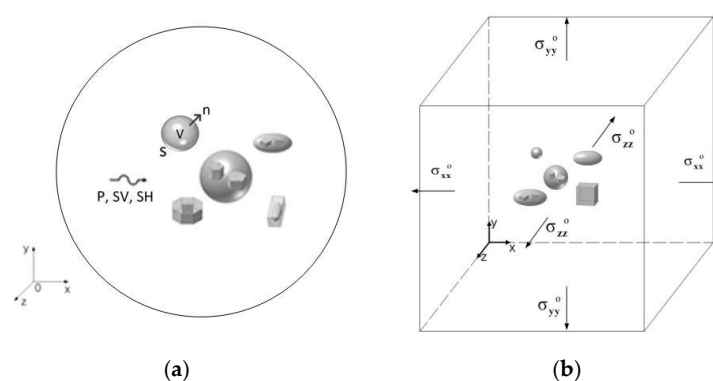


Figure 2. Geometry of the general (a) elastodynamic and (b) elastostatic problem.

Let $u_m^0(\mathbf{x}, \omega)e^{-i\omega t}$ signify the m th component of the displacement vector as a result of the incident field at \mathbf{x} in the absence of the inhomogeneities. Let $u_m(\mathbf{x}, \omega)e^{-i\omega t}$ signify the same within the inhomogeneities, where ω is the circular frequency of the waves. In the following example, we suppress the common time factor $e^{-i\omega t}$ and the explicit dependence of ω for all field quantities.

Mal and Knopoff [9] showed that the elastodynamic displacement $u_m(\mathbf{x})$, within the composite, fulfills the volume integral equation:

$$u_m(\mathbf{x}) = u_m^0(\mathbf{x}) + \int_R [\delta\rho \cdot \omega^2 \cdot g_i^m(\xi, \mathbf{x}) \cdot u_i(\xi) - \delta c_{ijkl} \cdot g_{i,j}^m(\xi, \mathbf{x}) \cdot u_{k,l}(\xi)] \cdot d\xi \quad (1)$$

where the integral is over entire space R , $\delta\rho$ and δc_{ijkl} show differences in the densities and the fourth-order elasticity tensors of the inhomogeneities and the unbounded matrix material: $\delta\rho = \rho^{(1)} - \rho^{(2)}$ and $\delta c_{ijkl} = c_{ijkl}^{(1)} - c_{ijkl}^{(2)}$. Since $c_{ijkl} = c_{jikl} = c_{ijlk} = c_{klij}$ ($i, j, k, l = 1, 2, 3$), c_{ijkl} can be reduced as $c_{\alpha\beta}$ ($\alpha, \beta = 1, 6$). The value $g_i^m(\xi, \mathbf{x})$ denotes the elastodynamic Green's function for the unbounded homogeneous matrix material. The value $g_i^m(\xi, \mathbf{x})$ stands for the i th displacement component at the point ξ as a result of unit concentrated force, $e_m e^{-i\omega t}$, at the point \mathbf{x} in the m th direction. It should be noted that the symbol e_m represents a unit vector in the m th direction. $u_{k,l}(\xi)$ represents the strain field inside the inhomogeneities. A detailed expression of three-dimensional elastostatic $g_{i,j}^m(\xi, \mathbf{x})$ will be in a later section.

The geometry of the general elastostatic problem is shown in Figure 2b. Lee and Mal [4] showed that the elastostatic displacement, $u_m(\mathbf{x})$, within the composite, fulfills the volume integral equation:

$$u_m(\mathbf{x}) = u_m^0(\mathbf{x}) - \int_R \delta c_{ijkl} \cdot g_{i,j}^m(\xi, \mathbf{x}) \cdot u_{k,l}(\xi) \cdot d\xi \quad (2)$$

where the integral is over entire space R and $\delta c_{ijkl} = c_{ijkl}^{(1)} - c_{ijkl}^{(2)}$. The value $g_i^m(\xi, \mathbf{x})$ is the elastostatic Green's function (or Kelvin's solution) for the unbounded homogeneous matrix material. The value $g_i^m(\xi, \mathbf{x})$ stands for the i th displacement component at the point ξ as a result of unit concentrated force at the point \mathbf{x} in the m th direction. The elastodynamic volume integral Equation (1) requires $g_i^m(\xi, \mathbf{x})$ and $g_{i,j}^m(\xi, \mathbf{x})$ while the elastostatic volume integral Equation (2) requires only $g_{i,j}^m(\xi, \mathbf{x})$. This is in contrast to the BEM.

In Equations (1) and (2), the summation convention and comma notation have been utilized and we differentiate them with respect to the integration variable ξ_i . It is evident that the integrand is non-zero within the inhomogeneities only, since $\delta c_{ijkl} = 0$, outside the inhomogeneities.

In Equations (1) and (2), \mathbf{x} represents a field point while ξ represents a point inside and on the boundary of the inhomogeneities (see Figure 3). Here, the field point is an exterior point or a point inside and on the boundary of the inhomogeneities. The field point (\mathbf{x}) and the point inside and on the boundary of the inhomogeneities (ξ) are independent of each other.

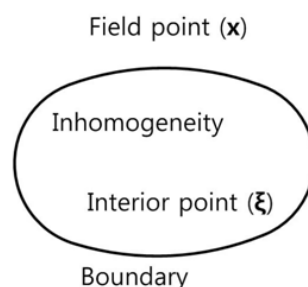


Figure 3. The field point and the interior point (including the boundary point).

If \mathbf{x} lies in the domain occupied by the inhomogeneities, then Equations (1) and (2) are integro-differential equations for the unknown displacement vector $\mathbf{u}(\mathbf{x})$ within the inhomogeneities, which can, in principle, be resolved through the solution of Equations (1) and (2). It is extremely

challenging and sometimes impossible to solve systems of linear equations analytically even within the presence of a single inhomogeneity of arbitrary shape. An algorithm based on the discretization of Equations (1) and (2) was developed by Lee and Mal [4,5] to compute numerically the unknown displacement vector $\mathbf{u}(\mathbf{x})$ by discretizing the inhomogeneities utilizing standard finite elements. Once $\mathbf{u}(\mathbf{x})$ inside the inhomogeneities is determined, the displacement field outside the inhomogeneities can be acquired from Equations (1) and (2) by assessing the integral. The stress field inside and outside the inhomogeneities can also be resolved without difficulty. Details of the numerical treatment of Equations (1) and (2) can be seen in references [5,10,11] for plane elastodynamic problems and in Lee and Mal [4] for plane elastostatic problems. Further mathematical detailing of the elastostatic VIEM can also be seen in Section 4.3 from the book “Volume Integral Equation Method” by Buryachenko [12]. A general description of the volume integral equation method can be viewed in Chapter 4 entitled “Volume Integral Equation Method (VIEM)” written by the first author of this paper, contained in the book “Advances in Computers and Information in Engineering Research, Vol. 2”, edited by Michopoulos et al. (eds.) [13].

It should be noted that Lee and his co-workers e.g., [4,5,7,10,11,14] have been developing the VIEM based on numerical modeling and analysis, while Buryachenko e.g., [12,15,16] has been performing research more mathematically.

In Section 3.1 of the reference [16], Buryachenko pointed out that “the VIEM was quite time-consuming and no optimized commercial software existed for its application.” Standard parallel programming, such as MPI (message passing interface), has been utilized to speed up computation in the VIEM. The parallel volume integral equation method (PVIEM) enabled us to investigate more complicated multiple anisotropic inhomogeneity problems elastostatically or elastodynamically. Since there is no commercial software for the VIEM, we are developing a VIEMAP (volume integral equation method application program). This VIEM modeling software includes a pre-processor, a solver and a post-processor, which are adapted to solve multiple isotropic/anisotropic inhomogeneity problems more easily and efficiently.

The authors intend to help university researchers and college students in undergraduate degree programs make VIEM models using the VIEMAP more conveniently than the finite element method and solve multiple isotropic/anisotropic inhomogeneity problems in an unbounded isotropic media more accurately and easily than the boundary element method.

3. Numerical Analysis Based On the Three-Dimensional Volume Integral Equation Method

3.1. A Single Cubic Inhomogeneity Problem

In this section, in order to introduce the volume integral equation method for three-dimensional elastostatic problems, we consider a single isotropic or orthotropic cubic inhomogeneity in an unbounded isotropic matrix subject to uniform remote tensile loading, σ_{xx}^0 , as shown in Figure 4 (see also Figure 2b).

We first consider a single isotropic cubic inhomogeneity ($-4 \text{ mm} \leq x, y, z \leq 4 \text{ mm}$) in the unbounded isotropic matrix. Four models with a different number of quadratic hexahedral elements for the isotropic inhomogeneity are used for the convergence test; Model $8 \times 8 \times 8$ (512 elements), Model $10 \times 10 \times 10$ (1000 elements), Model $14 \times 14 \times 14$ (2744 elements) and Model $16 \times 16 \times 16$ (4096 elements). Figure 4 shows typical discretized models used in the VIEM [17].

Next we consider a single orthotropic cubic inhomogeneity ($-4 \text{ mm} \leq x, y, z \leq 4 \text{ mm}$) in the unbounded isotropic matrix. The same four models for the isotropic inhomogeneity are used for the orthotropic inhomogeneity.

The elastic constants for the isotropic matrix, the isotropic inhomogeneity and three different kinds of orthotropic inhomogeneity are listed in Tables 1 and 2. In order to distinguish different material properties easily, we assign a distinct material name (mat_01, mat_02, mat_03, —) to each material.

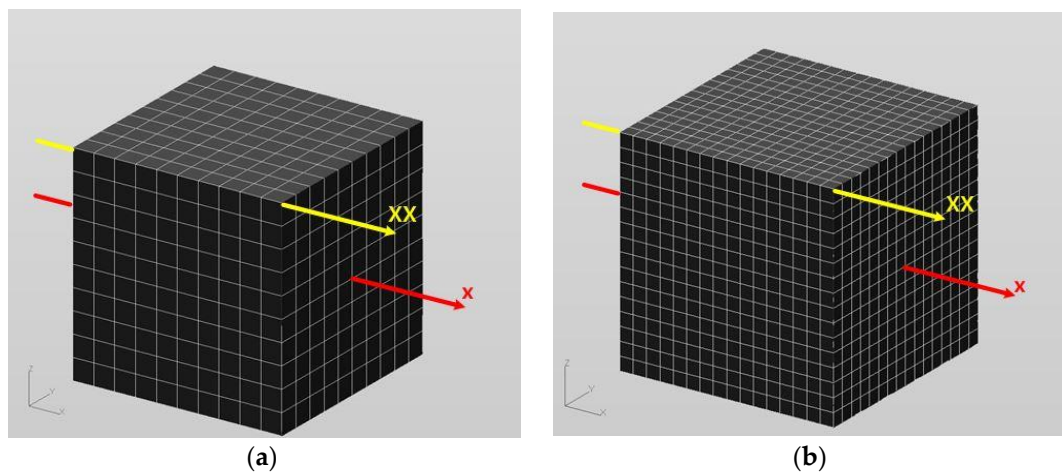


Figure 4. Typical discretized cubic models ($-4 \text{ mm} \leq x, y, z \leq 4 \text{ mm}$) in the volume integral equation method (VIEM). (a) A single cube (Model₁₀ \times 10 \times 10); (b) A single cube (Model₁₆ \times 16 \times 16).

Table 1. Material properties of the isotropic matrix and the isotropic inhomogeneity.

(Unit: GPa)	Isotropic Matrix (mat_01)	Isotropic Inhomogeneity (mat_01)
λ	67.34	176.06
μ	37.88	176.06

Table 2. Material properties of the isotropic matrix and the isotropic and orthotropic cubic inhomogeneity.

	Isotropic Matrix (mat_01, 02, 03, 04)	Isotropic Inhomogeneity (mat_01)	Orthotropic Inhomogeneity #1 (mat_02)	Orthotropic Inhomogeneity #2 (mat_03)	Orthotropic Inhomogeneity #3 (mat_04)
c_{11} [GPa]	143.10	528.18	139.54	279.08	418.61
c_{12} [GPa]	67.34	176.06	3.90	7.80	11.70
c_{13} [GPa]	67.34	176.06	3.90	7.80	11.70
c_{22} [GPa]	143.10	528.18	15.28	30.56	45.83
c_{23} [GPa]	67.34	176.06	3.29	6.59	9.88
c_{33} [GPa]	143.10	528.18	15.28	30.56	45.83
c_{44} [GPa]	37.88	176.06	5.90	11.80	17.70
c_{55} [GPa]	37.88	176.06	5.90	11.80	17.70
c_{66} [GPa]	37.88	176.06	5.90	11.80	17.70

3.1.1. Volume Integral Equation for an Unbounded Isotropic Matrix Containing a Single Isotropic Cubic Inhomogeneity

The coordinate axes are x_1, x_2, x_3 . The stress–strain relationships ($\sigma_\alpha = c_{\alpha\beta} \varepsilon_\beta$ ($\alpha, \beta = 1, 6$)) for the isotropic inhomogeneities can be expressed in the form:

$$\begin{Bmatrix} \sigma_1 \\ \sigma_2 \\ \sigma_3 \\ \sigma_4 \\ \sigma_5 \\ \sigma_6 \end{Bmatrix} = \begin{bmatrix} \lambda + 2\mu & \lambda & \lambda & 0 & 0 & 0 \\ \lambda & \lambda + 2\mu & \lambda & 0 & 0 & 0 \\ \lambda & \lambda & \lambda + 2\mu & 0 & 0 & 0 \\ 0 & 0 & 0 & \mu & 0 & 0 \\ 0 & 0 & 0 & 0 & \mu & 0 \\ 0 & 0 & 0 & 0 & 0 & \mu \end{bmatrix} \begin{Bmatrix} \varepsilon_1 \\ \varepsilon_2 \\ \varepsilon_3 \\ \varepsilon_4 \\ \varepsilon_5 \\ \varepsilon_6 \end{Bmatrix}. \quad (3)$$

It should be noted that the stress–strain relationships are also referred to as constitutive equations.

In Equation (3), the stiffness constants c_{ij} are related to the engineering elastic constants through $c_{11} = c_{22} = c_{33} = (\lambda + 2\mu)$, $c_{12} = c_{13} = c_{23} = \lambda$, and $c_{44} = c_{55} = c_{66} = \mu$.

The displacement components in the volume integral Equation (2) for multiple isotropic inhomogeneities can be expressed in the form:

$$\begin{aligned} u_1(x) = & u_1^0(x) - \int_V \{ \delta(\lambda + 2\mu) g_{1,1}^1 u_{1,1} + \delta\lambda (g_{1,1}^1 u_{2,2} + g_{2,2}^1 u_{1,1}) + \delta\lambda (g_{1,1}^1 u_{3,3} + g_{3,3}^1 u_{1,1}) \\ & + \delta(\lambda + 2\mu) g_{2,2}^1 u_{2,2} + \delta\lambda (g_{2,2}^1 u_{3,3} + g_{3,3}^1 u_{2,2}) + \delta(\lambda + 2\mu) g_{3,3}^1 u_{3,3} \\ & + \delta\mu [g_{2,3}^1 (u_{2,3} + u_{3,2}) + g_{3,2}^1 (u_{2,3} + u_{3,2})] \\ & + \delta\mu [g_{1,3}^1 (u_{1,3} + u_{3,1}) + g_{3,1}^1 (u_{1,3} + u_{3,1})] \\ & + \delta\mu [g_{1,2}^1 (u_{1,2} + u_{2,1}) + g_{2,1}^1 (u_{1,2} + u_{2,1})] \} d\xi_1 d\xi_2 d\xi_3 \end{aligned} \quad (4)$$

$$\begin{aligned} u_2(x) = & u_2^0(x) - \int_V \{ \delta(\lambda + 2\mu) g_{1,1}^2 u_{1,1} + \delta\lambda (g_{1,1}^2 u_{2,2} + g_{2,2}^2 u_{1,1}) + \delta\lambda (g_{1,1}^2 u_{3,3} + g_{3,3}^2 u_{1,1}) \\ & + \delta(\lambda + 2\mu) g_{2,2}^2 u_{2,2} + \delta\lambda (g_{2,2}^2 u_{3,3} + g_{3,3}^2 u_{2,2}) + \delta(\lambda + 2\mu) g_{3,3}^2 u_{3,3} \\ & + \delta\mu [g_{2,3}^2 (u_{2,3} + u_{3,2}) + g_{3,2}^2 (u_{2,3} + u_{3,2})] \\ & + \delta\mu [g_{1,3}^2 (u_{1,3} + u_{3,1}) + g_{3,1}^2 (u_{1,3} + u_{3,1})] \\ & + \delta\mu [g_{1,2}^2 (u_{1,2} + u_{2,1}) + g_{2,1}^2 (u_{1,2} + u_{2,1})] \} d\xi_1 d\xi_2 d\xi_3 \end{aligned} \quad (5)$$

$$\begin{aligned} u_3(x) = & u_3^0(x) - \int_V \{ \delta(\lambda + 2\mu) g_{1,1}^3 u_{1,1} + \delta\lambda (g_{1,1}^3 u_{2,2} + g_{2,2}^3 u_{1,1}) + \delta\lambda (g_{1,1}^3 u_{3,3} + g_{3,3}^3 u_{1,1}) \\ & + \delta(\lambda + 2\mu) g_{2,2}^3 u_{2,2} + \delta\lambda (g_{2,2}^3 u_{3,3} + g_{3,3}^3 u_{2,2}) + \delta(\lambda + 2\mu) g_{3,3}^3 u_{3,3} \\ & + \delta\mu [g_{2,3}^3 (u_{2,3} + u_{3,2}) + g_{3,2}^3 (u_{2,3} + u_{3,2})] \\ & + \delta\mu [g_{1,3}^3 (u_{1,3} + u_{3,1}) + g_{3,1}^3 (u_{1,3} + u_{3,1})] \\ & + \delta\mu [g_{1,2}^3 (u_{1,2} + u_{2,1}) + g_{2,1}^3 (u_{1,2} + u_{2,1})] \} d\xi_1 d\xi_2 d\xi_3 \end{aligned} \quad (6)$$

where $u_1(x)$, $u_2(x)$ and $u_3(x)$ are the three-dimensional displacement components, $\delta c_{\alpha\beta} = c_{\alpha\beta}^{(1)} - c_{\alpha\beta}^{(2)}$ ($\alpha, \beta = 1, 6$), where $c_{\alpha\beta}^{(1)}$ represent the elastic stiffness constants of the isotropic inhomogeneities while $c_{\alpha\beta}^{(2)}$ denote those for the isotropic matrix material; $\delta c_{11} = \delta c_{22} = \delta c_{33} = (\lambda_1 + 2\mu_1) - (\lambda_2 + 2\mu_2)$, $\delta c_{12} = \delta c_{13} = \delta c_{23} = \lambda_1 - \lambda_2$, and $\delta c_{44} = \delta c_{55} = \delta c_{66} = \mu_1 - \mu_2$.

In Equations (4)–(6), $g_i^m(\xi, x)$ shows the Green's function for the unbounded isotropic matrix material and is presented by Banerjee [18] and Pao and Varadarajulu [19] as:

$$\begin{aligned} g_1^1 &= \frac{1}{16\pi(1-\nu)\mu r} \left[\frac{(x_1 - \xi_1)^2}{r^2} + (3 - 4\nu) \right] \\ g_2^1 &= g_1^2 = \frac{1}{16\pi(1-\nu)\mu r} \left[\frac{(x_1 - \xi_1)(x_2 - \xi_2)}{r^2} \right] \\ g_3^1 &= g_1^3 = \frac{1}{16\pi(1-\nu)\mu r} \left[\frac{(x_1 - \xi_1)(x_3 - \xi_3)}{r^2} \right] \\ g_2^2 &= \frac{1}{16\pi(1-\nu)\mu r} \left[\frac{(x_2 - \xi_2)^2}{r^2} + (3 - 4\nu) \right] \\ g_3^2 &= g_2^3 = \frac{1}{16\pi(1-\nu)\mu r} \left[\frac{(x_2 - \xi_2)(x_3 - \xi_3)}{r^2} \right] \\ g_3^3 &= \frac{1}{16\pi(1-\nu)\mu r} \left[\frac{(x_3 - \xi_3)^2}{r^2} + (3 - 4\nu) \right] \end{aligned} \quad (7)$$

where $r = |\mathbf{x} - \boldsymbol{\xi}| = \sqrt{(x_1 - \xi_1)^2 + (x_2 - \xi_2)^2 + (x_3 - \xi_3)^2}$, ν is Poisson's ratio, and μ is the shear modulus.

Also, $g_{i,j}^m(\xi, x)$ is presented as:

$$\begin{aligned}
 g_{1,1}^1 &= \frac{1}{16\pi(1-\nu)\mu r^2} \left\{ \frac{3(x_1 - \xi_1)^3}{r^3} + \frac{(1-4\nu)(x_1 - \xi_1)}{r} \right\} \\
 g_{1,2}^1 &= \frac{1}{16\pi(1-\nu)\mu r^2} \left\{ \frac{3(x_1 - \xi_1)^2(x_2 - \xi_2)}{r^3} + \frac{(3-4\nu)(x_2 - \xi_2)}{r} \right\} \\
 g_{1,3}^1 &= \frac{1}{16\pi(1-\nu)\mu r^2} \left\{ \frac{3(x_1 - \xi_1)^2(x_3 - \xi_3)}{r^3} + \frac{(3-4\nu)(x_3 - \xi_3)}{r} \right\} \\
 g_{2,1}^1 &= g_{1,1}^2 = \frac{1}{16\pi(1-\nu)\mu r^2} \left\{ \frac{3(x_1 - \xi_1)^2(x_2 - \xi_2)}{r^3} - \frac{(x_2 - \xi_2)}{r} \right\} \\
 g_{2,2}^1 &= g_{1,2}^2 = \frac{1}{16\pi(1-\nu)\mu r^2} \left\{ \frac{3(x_1 - \xi_1)(x_2 - \xi_2)^2}{r^3} - \frac{(x_1 - \xi_1)}{r} \right\} \\
 g_{2,3}^1 &= g_{1,3}^2 = \frac{1}{16\pi(1-\nu)\mu r^2} \left\{ \frac{3(x_1 - \xi_1)(x_2 - \xi_2)(x_3 - \xi_3)}{r^3} \right\} \\
 g_{3,1}^1 &= g_{1,1}^3 = \frac{1}{16\pi(1-\nu)\mu r^2} \left\{ \frac{3(x_1 - \xi_1)^2(x_3 - \xi_3)}{r^3} - \frac{(x_3 - \xi_3)}{r} \right\} \\
 g_{3,2}^1 &= g_{1,2}^3 = \frac{1}{16\pi(1-\nu)\mu r^2} \left\{ \frac{3(x_1 - \xi_1)(x_2 - \xi_2)(x_3 - \xi_3)}{r^3} \right\} \\
 g_{3,3}^1 &= g_{1,3}^3 = \frac{1}{16\pi(1-\nu)\mu r^2} \left\{ \frac{3(x_1 - \xi_1)(x_3 - \xi_3)^2}{r^3} - \frac{(x_1 - \xi_1)}{r} \right\} \\
 g_{2,1}^2 &= \frac{1}{16\pi(1-\nu)\mu r^2} \left\{ \frac{3(x_1 - \xi_1)(x_2 - \xi_2)^2}{r^3} + \frac{(3-4\nu)(x_1 - \xi_1)}{r} \right\} \\
 g_{2,2}^2 &= \frac{1}{16\pi(1-\nu)\mu r^2} \left\{ \frac{3(x_2 - \xi_2)^3}{r^3} + \frac{(1-4\nu)(x_2 - \xi_2)}{r} \right\} \\
 g_{2,3}^2 &= \frac{1}{16\pi(1-\nu)\mu r^2} \left\{ \frac{3(x_2 - \xi_2)^2(x_3 - \xi_3)}{r^3} + \frac{(3-4\nu)(x_3 - \xi_3)}{r} \right\} \\
 g_{3,1}^2 &= g_{2,1}^3 = \frac{1}{16\pi(1-\nu)\mu r^2} \left\{ \frac{3(x_1 - \xi_1)(x_2 - \xi_2)(x_3 - \xi_3)}{r^3} \right\} \\
 g_{3,2}^2 &= g_{2,2}^3 = \frac{1}{16\pi(1-\nu)\mu r^2} \left\{ \frac{3(x_2 - \xi_2)^2(x_3 - \xi_3)}{r^3} - \frac{(x_3 - \xi_3)}{r} \right\} \\
 g_{3,3}^2 &= g_{2,3}^3 = \frac{1}{16\pi(1-\nu)\mu r^2} \left\{ \frac{3(x_2 - \xi_2)(x_3 - \xi_3)^2}{r^3} - \frac{(x_2 - \xi_2)}{r} \right\} \\
 g_{3,1}^3 &= \frac{1}{16\pi(1-\nu)\mu r^2} \left\{ \frac{3(x_1 - \xi_1)(x_3 - \xi_3)^2}{r^3} + \frac{(3-4\nu)(x_1 - \xi_1)}{r} \right\} \\
 g_{3,2}^3 &= \frac{1}{16\pi(1-\nu)\mu r^2} \left\{ \frac{3(x_2 - \xi_2)(x_3 - \xi_3)^2}{r^3} + \frac{(3-4\nu)(x_2 - \xi_2)}{r} \right\}
 \end{aligned}$$

$$g_{3,3}^3 = \frac{1}{16\pi(1-\nu)\mu r^2} \left\{ \frac{3(x_3 - \xi_3)^3}{r^3} + \frac{(1-4\nu)(x_3 - \xi_3)}{r} \right\} \quad (8)$$

It should be noted that for the applied uniformly remote stress, the displacement vector u^o is of the form:

$$u_1^o = c_1 x, u_2^o = c_2 y, u_3^o = c_3 z \quad (9)$$

where the constants C_1 – C_3 are related to the tensile and shear components of the applied uniformly remote stress.

3.1.2. Volume Integral Equation for an Unbounded Isotropic Matrix Containing a Single Orthotropic Cubic Inhomogeneity

Let the coordinate axes x_1, x_2, x_3 be taken parallel to the symmetry axes of the orthotropic material. The constitutive equations for the orthotropic inhomogeneities can be expressed in the form:

$$\begin{pmatrix} \sigma_1 \\ \sigma_2 \\ \sigma_3 \\ \sigma_4 \\ \sigma_5 \\ \sigma_6 \end{pmatrix} = \begin{bmatrix} c_{11} & c_{12} & c_{13} & 0 & 0 & 0 \\ c_{12} & c_{22} & c_{23} & 0 & 0 & 0 \\ c_{13} & c_{23} & c_{33} & 0 & 0 & 0 \\ 0 & 0 & 0 & c_{44} & 0 & 0 \\ 0 & 0 & 0 & 0 & c_{55} & 0 \\ 0 & 0 & 0 & 0 & 0 & c_{66} \end{bmatrix} \begin{pmatrix} \varepsilon_1 \\ \varepsilon_2 \\ \varepsilon_3 \\ \varepsilon_4 \\ \varepsilon_5 \\ \varepsilon_6 \end{pmatrix} \quad (10)$$

The stiffness constants c_{ij} are related to the engineering elastic constants through:

$$c_{11} = \frac{1-\nu_{23}\nu_{32}}{E_2 E_3 \Delta}, \quad c_{12} = \frac{\nu_{21}+\nu_{31}\nu_{23}}{E_2 E_3 \Delta} = c_{21}, \quad c_{13} = \frac{\nu_{31}+\nu_{21}\nu_{32}}{E_2 E_3 \Delta} = c_{31}, \quad c_{22} = \frac{1-\nu_{31}\nu_{13}}{E_3 E_1 \Delta}, \quad (11)$$

$$c_{23} = \frac{\nu_{32}+\nu_{31}\nu_{12}}{E_3 E_1 \Delta} = c_{32}, \quad c_{33} = \frac{1-\nu_{12}\nu_{21}}{E_1 E_2 \Delta}, \quad c_{44} = \mu_{23}, \quad c_{55} = \mu_{31}, \quad c_{66} = \mu_{12},$$

where,

$$\Delta = \frac{1 - \nu_{12}\nu_{21} - \nu_{23}\nu_{32} - \nu_{31}\nu_{13} - 2\nu_{12}\nu_{23}\nu_{31}}{E_1 E_2 E_3}. \quad (12)$$

In the above equations, E_1, E_2, E_3 are Young's moduli in 1, 2 and 3 directions, respectively, μ_{23}, μ_{31} and μ_{12} are the shear moduli in the 2-3, 3-1 and 1-2 planes, respectively. ν_{ij} is Poisson's ratio for transverse strain in the j -direction when stressed in the i -direction. It should be noted that the elastic moduli satisfy the reciprocal $\nu_{ij}/E_i = \nu_{ji}/E_j$.

The displacement components in the volume integral Equation (2) for multiple orthotropic inhomogeneities can be expressed in the form:

$$u_1(x) = u_1^o(x) - \int_V \left\{ \delta c_{11} g_{1,1}^1 u_{1,1} + \delta c_{12} (g_{1,1}^1 u_{2,2} + g_{2,2}^1 u_{1,1}) + \delta c_{13} (g_{1,1}^1 u_{3,3} + g_{3,3}^1 u_{1,1}) \right. \\ \left. + \delta c_{22} g_{2,2}^1 u_{2,2} + \delta c_{23} (g_{2,2}^1 u_{3,3} + g_{3,3}^1 u_{2,2}) + \delta c_{33} g_{3,3}^1 u_{3,3} \right. \\ \left. + \delta c_{44} [g_{2,3}^1 (u_{2,3} + u_{3,2}) + g_{3,2}^1 (u_{2,3} + u_{3,2})] \right. \\ \left. + \delta c_{55} [g_{1,3}^1 (u_{1,3} + u_{3,1}) + g_{3,1}^1 (u_{1,3} + u_{3,1})] \right. \\ \left. + \delta c_{66} [g_{1,2}^1 (u_{1,2} + u_{2,1}) + g_{2,1}^1 (u_{1,2} + u_{2,1})] \right\} d\xi_1 d\xi_2 d\xi_3 \quad (13)$$

$$u_2(x) = u_2^o(x) - \int_V \left\{ \delta c_{11} g_{1,1}^2 u_{1,1} + \delta c_{12} (g_{1,1}^2 u_{2,2} + g_{2,2}^2 u_{1,1}) + \delta c_{13} (g_{1,1}^2 u_{3,3} + g_{3,3}^2 u_{1,1}) \right. \\ \left. + \delta c_{22} g_{2,2}^2 u_{2,2} + \delta c_{23} (g_{2,2}^2 u_{3,3} + g_{3,3}^2 u_{2,2}) + \delta c_{33} g_{3,3}^2 u_{3,3} \right. \\ \left. + \delta c_{44} [g_{2,3}^2 (u_{2,3} + u_{3,2}) + g_{3,2}^2 (u_{2,3} + u_{3,2})] \right. \\ \left. + \delta c_{55} [g_{1,3}^2 (u_{1,3} + u_{3,1}) + g_{3,1}^2 (u_{1,3} + u_{3,1})] \right. \\ \left. + \delta c_{66} [g_{1,2}^2 (u_{1,2} + u_{2,1}) + g_{2,1}^2 (u_{1,2} + u_{2,1})] \right\} d\xi_1 d\xi_2 d\xi_3 \quad (14)$$

and,

$$\begin{aligned}
 u_3(x) = & u_3^o(x) - \int_V \{ \delta c_{11} g_{1,1}^3 u_{1,1} + \delta c_{12} (g_{1,1}^3 u_{2,2} + g_{2,2}^3 u_{1,1}) + \delta c_{13} (g_{1,1}^3 u_{3,3} + g_{3,3}^3 u_{1,1}) \\
 & + \delta c_{22} g_{2,2}^3 u_{2,2} + \delta c_{23} (g_{2,2}^3 u_{3,3} + g_{3,3}^3 u_{2,2}) + \delta c_{33} g_{3,3}^3 u_{3,3} \\
 & + \delta c_{44} [g_{2,3}^3 (u_{2,3} + u_{3,2}) + g_{3,2}^3 (u_{2,3} + u_{3,2})] \\
 & + \delta c_{55} [g_{1,3}^3 (u_{1,3} + u_{3,1}) + g_{3,1}^3 (u_{1,3} + u_{3,1})] \\
 & + \delta c_{66} [g_{1,2}^3 (u_{1,2} + u_{2,1}) + g_{2,1}^3 (u_{1,2} + u_{2,1})] \} d\xi_1 d\xi_2 d\xi_3
 \end{aligned} \quad (15)$$

where $u_1(x)$, $u_2(x)$ and $u_3(x)$ are the three-dimensional displacement components, $\delta c_{\alpha\beta} = c_{\alpha\beta}^{(1)} - c_{\alpha\beta}^{(2)}$ ($\alpha, \beta = 1, 6$), where $c_{\alpha\beta}^{(1)}$ represent the elastic stiffness constants of the orthotropic inhomogeneities while $c_{\alpha\beta}^{(2)}$ denote those for the isotropic matrix material; $\delta c_{11} = c_{11} - (\lambda_2 + 2\mu_2)$, $\delta c_{22} = c_{22} - (\lambda_2 + 2\mu_2)$, $\delta c_{33} = c_{33} - (\lambda_2 + 2\mu_2)$, $\delta c_{12} = c_{12} - \lambda_2$, $\delta c_{13} = c_{13} - \lambda_2$, $\delta c_{23} = c_{23} - \lambda_2$, and $\delta c_{44} = c_{44} - \mu_2$, $\delta c_{55} = c_{55} - \mu_2$, $\delta c_{66} = c_{66} - \mu_2$.

In Equations (13)–(15), $g_i^m(\xi, x)$ is Green's function for the unbounded isotropic matrix material. Thus, the VIEM does not need to use Green's function for the orthotropic material of the inhomogeneity.

3.1.3. Numerical Formulation

The integrands in the volume integral Equations (4)–(6) and Equations (13)–(15) contain singularities with different orders due to the singular characteristics of Green's function at $x = \xi$ (i.e., $r = 0$), and the evaluation of the singular integrals requires special attention. In general, $g_i^m(\xi, x)$ behaves as $1/r$ while its derivatives behave as $1/r^2$ as $r \rightarrow 0$. It ought to be noted that the VIEM involves only $g_i^m(\xi, x)$ for the isotropic matrix and its derivatives. By contrast, the BEM involves Green's function for these and for the anisotropic inhomogeneities and their derivatives. The singularities in the VIEM are weaker (integrable) when compared with those in the BEM. Therefore, we have utilized the direct integration scheme introduced by Li et al. [20] after reasonable adjustments to address these singularities in the integrands.

The order of singularity of the singular elements decreases by one degree with tetrahedron polar co-ordinates [20] in the VIEM. This strategy also converts weakly singular integrals into integrals over smooth functions. The tetrahedron polar co-ordinates are applied to quadratic, hexahedral, isoparametric singular elements as follows: (1) In Figure 5a, Ω^f stands for the quadratic hexahedral element indicating the interior of the considered body. Ω^f is associated with a global three-dimensional Cartesian coordinate system. Ω^f is mapped onto a cube $\Omega^{f'}$ of side-length 2, characterized by the local three-dimensional Cartesian coordinates, ξ_1 , ξ_2 and ξ_3 . (2) If the singular point is located at a corner node, $\Omega^{f'}$ is divided into two triangular prisms, $\Omega_1^{f'}$ and $\Omega_2^{f'}$, as shown in Figure 5b. If the singular point is located at a midside node, then $\Omega^{f'}$ is divided into three triangular prisms, $\Omega_1^{f'}$, $\Omega_2^{f'}$ and $\Omega_3^{f'}$, as shown in Figure 5b. (3) A subdivision of each triangular prism is divided into three tetrahedral subcells as shown in Figure 5c. (4) Each subcell maps onto a unit cube, applying the tetrahedron polar coordinates [20]; the subcell $\Omega_{11}^{f'}$ maps onto $\Omega_{11}^{f''}$. Subsequently, $\Omega_{11}^{f''}$ maps onto $\Omega_{11}^{f'''}$ in Figure 5d. The last mapping stands for a linear transformation carrying out numerical integrations in a standard way.

Figure 6 shows a typical hexahedral element used in the VIEM. Standard 20-node quadratic hexahedral elements were used in finite element discretization of the VIEM models. Figure 7 shows a detailed explanation for a subdivision of each triangular prism into three tetrahedral subcells after a subdivision of $\Omega^{f'}$ into two ($\Omega_1^{f'}$ and $\Omega_2^{f'}$) or three triangular prisms ($\Omega_1^{f'}$, $\Omega_2^{f'}$ and $\Omega_3^{f'}$) (see Figure 5b) for the hexahedral element used in the VIEM (Figure 6).

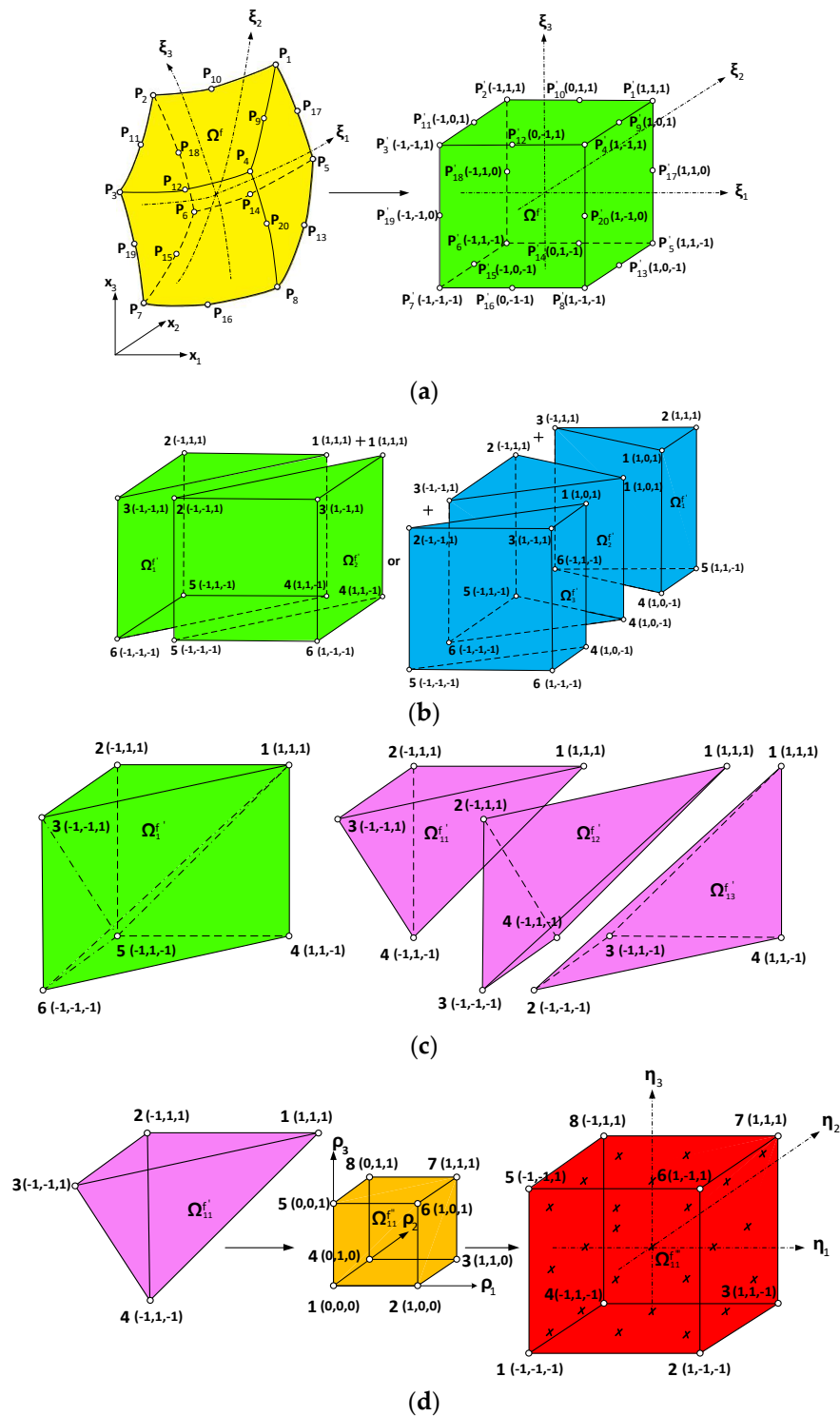


Figure 5. Application of the tetrahedron polar co-ordinates to quadratic, hexahedral, isoparametric singular elements [20]. (a) Mapping of Ω^f onto $\Omega^{f'}$; (b) subdivision of $\Omega^{f'}$ at the singular point 1; (c) subdivision of triangular prism $\Omega_1^{f'}$ into three tetrahedral; (d) mapping of $\Omega_{11}^{f'}$ onto $\Omega_{11}^{f''}$ and of $\Omega_{11}^{f''}$ onto $\Omega_{11}^{f'''}$.

Tables 3 and 4 show a detailed explanation for a subdivision of each triangular prism into three tetrahedral subcells after a subdivision of $\Omega^{f'}$ into two or three triangular prisms (see Figure 5b,c), respectively, for the hexahedral element used in the VIEM (Figure 6). Table 3 shows a subdivision of each triangular prism into three tetrahedral subcells after a subdivision of $\Omega^{f'}$ into two triangular

prisms (see Figure 5b,c). This subdivision technique is applied to all the corner nodes, 1, 3, 5, 7, 13, 15, 17 and 19 of the hexahedral element shown in Figure 6. Thus, the total number of cases in Table 3 increases to 48 (8 nodes \times 6 cases). Table 4 shows a subdivision of each triangular prism into three tetrahedral subcells after a subdivision of Ω^f into three triangular prisms (see Figure 5b,c). The same subdivision technique is applied to all the midside nodes, 2, 4, 6, 8, 9, 10, 11, 12, 14, 16, 18 and 20 of the hexahedral element shown in Figure 6. Thus, the total number of cases in Table 4 rises to 108 (12 nodes \times 9 cases). It should be noted that, in Tables 3 and 4, 1, 2 or 1, 2 and 3 in the triangular prism column and 1, 2 and 3 in the tetrahedron column are arbitrarily selected. There is no particular order in the numbers, 1, 2 or 1, 2 and 3. Therefore, in order to compute singular integrals accurately, it is necessary to investigate 156 total cases (48 cases in Table 3 and 108 cases in Table 4) per hexahedral element.

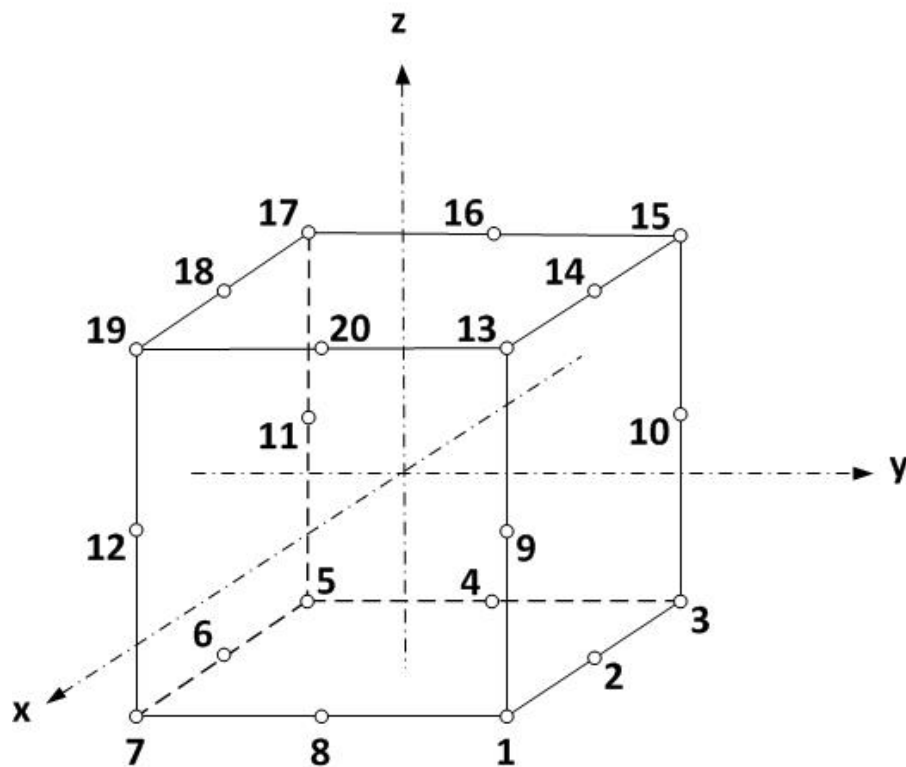


Figure 6. A typical quadratic hexahedral element used in the VIEM.

Table 3. A subdivision of each triangular prism into three tetrahedral subcells at each singular point after a subdivision of Ω^f into two triangular prisms (see Figure 5b,c). The singular point is located at the corner point of the hexahedral element shown in Figure 6.

Singular Point	Triangular Prism	Tetrahedron	Node 1	Node 2	Node 3	Node 4
1	1	1	1	5	7	19
		2	1	17	5	19
		3	1	13	17	19
	2	1	1	3	5	17
		2	1	15	3	17
		3	1	13	15	17

Table 3. Cont.

Singular Point	Triangular Prism	Tetrahedron	Node 1	Node 2	Node 3	Node 4
3	1	1	3	7	1	13
		2	3	19	7	13
		3	3	15	19	13
	2	1	3	5	7	19
		2	3	17	5	19
		3	3	15	17	19
5	1	1	5	7	1	19
		2	5	1	13	19
		3	5	13	17	19
	2	1	5	1	3	13
		2	5	3	15	13
		3	5	15	17	13
7	1	1	7	1	3	13
		2	7	3	15	13
		3	7	15	19	13
	2	1	7	3	5	15
		2	7	5	17	15
		3	7	17	19	15
13	1	1	13	17	15	3
		2	13	5	17	3
		3	13	1	5	3
	2	1	13	19	17	5
		2	13	7	19	5
		3	13	1	7	5
15	1	1	15	19	17	5
		2	15	7	19	5
		3	15	3	7	5
	2	1	15	13	19	7
		2	15	1	13	7
		3	15	3	1	7
17	1	1	17	15	13	3
		2	17	13	1	3
		3	17	1	5	3
	2	1	17	13	19	1
		2	17	19	7	1
		3	17	7	5	1
19	1	1	19	17	15	5
		2	19	15	3	5
		3	19	3	7	5
	2	1	19	15	13	3
		2	19	13	1	3
		3	19	1	7	3

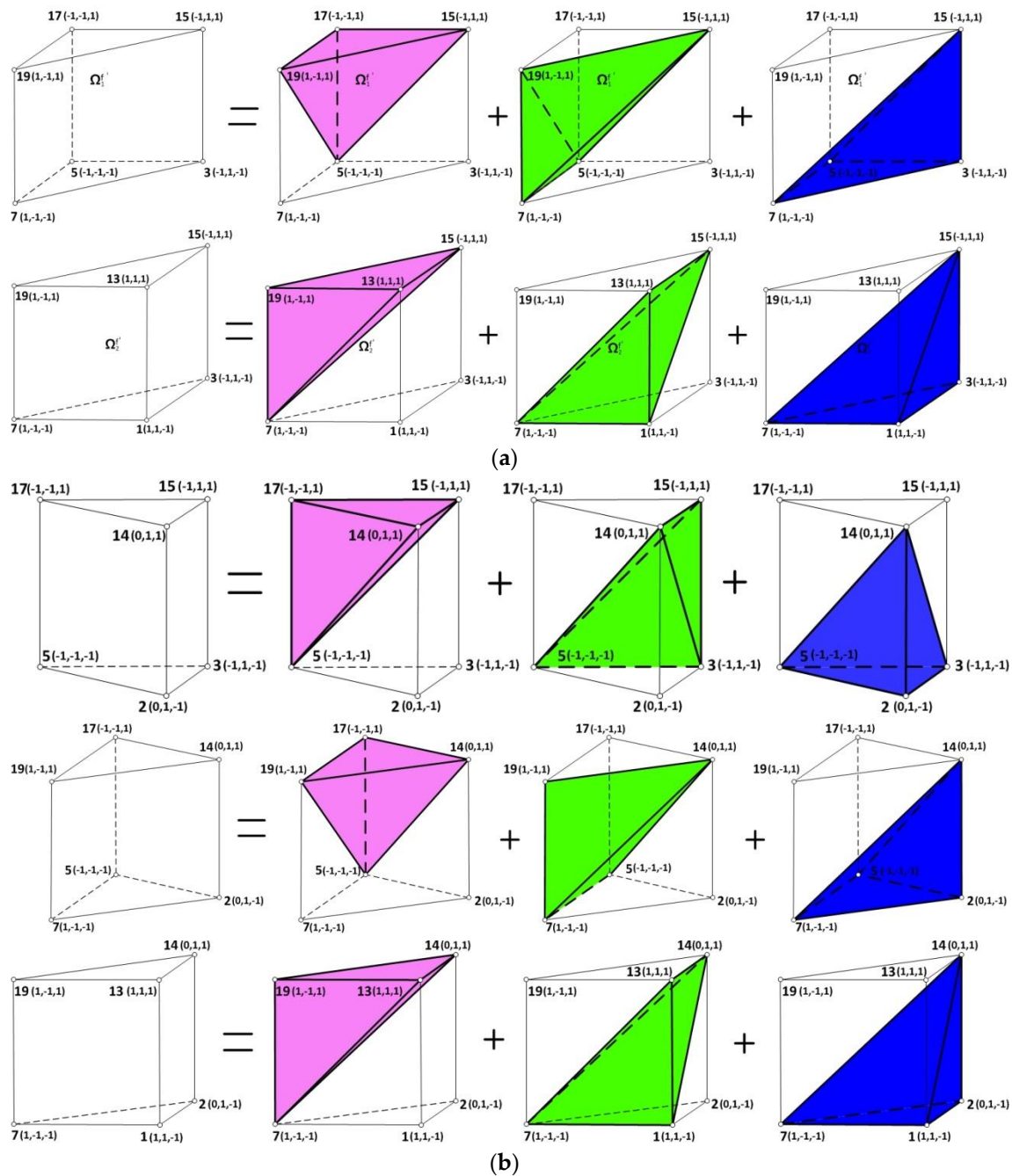


Figure 7. A subdivision of each triangular prism into three tetrahedral subcells after a subdivision of Ω^f into two or three triangular prisms (see Figure 5b,c). (a) A subdivision of each triangular prism into three tetrahedral subcells at the singular point 15 after a subdivision of Ω^f into two triangular prisms (Ω_1^f and Ω_2^f) (see Figure 5b,c); (b) a subdivision of each triangular prism into three tetrahedral subcells at the singular point 14 after a subdivision of Ω^f into three triangular prisms (Ω_1^f , Ω_2^f and Ω_3^f) (see Figure 5b,c).

Table 4. A subdivision of each triangular prism into three tetrahedral subcells at each singular point after a subdivision of Ω^f into three triangular prisms (see Figure 5b,c). The singular point is located at the midside of the hexahedral element shown in Figure 6.

Singular Point	Triangular Prism	Tetrahedron	Node 1	Node 2	Node 3	Node 4
2	1	1	2	3	5	15
		2	2	5	17	15
		3	2	17	14	15
	2	1	2	5	7	19
		2	2	17	5	19
		3	2	14	17	19
	3	1	2	7	1	13
		2	2	19	7	13
		3	2	14	19	13
4	1	1	4	1	3	13
		2	4	3	15	13
		3	4	15	16	13
	2	1	4	7	1	13
		2	4	19	7	13
		3	4	16	19	13
	3	1	4	5	7	19
		2	4	17	5	19
		3	4	16	17	19
6	1	1	6	3	5	15
		2	6	5	17	15
		3	6	17	18	15
	2	1	6	1	3	15
		2	6	13	1	15
		3	6	18	13	15
	3	1	6	7	1	13
		2	6	19	7	13
		3	6	18	19	13
8	1	1	8	1	3	15
		2	8	13	1	15
		3	8	20	13	15
	2	1	8	3	5	15
		2	8	5	17	15
		3	8	17	20	15
	3	1	8	5	7	17
		2	8	7	19	17
		3	8	19	20	17

Table 4. Cont.

Singular Point	Triangular Prism	Tetrahedron	Node 1	Node 2	Node 3	Node 4
9	1	1	9	13	15	17
		2	9	19	13	17
		3	9	12	19	17
	2	1	9	15	3	17
		2	9	3	5	17
		3	9	5	12	17
	3	1	9	3	1	5
		2	9	1	7	5
		3	9	7	12	5
10	1	1	10	13	15	19
		2	10	15	17	19
		3	10	17	11	19
	2	1	10	1	13	19
		2	10	7	1	19
		3	10	11	7	19
	3	1	10	3	1	7
		2	10	5	3	7
		3	10	11	5	7
11	1	1	11	17	19	13
		2	11	15	17	13
		3	11	10	15	13
	2	1	11	19	7	13
		2	11	7	1	13
		3	11	1	10	13
	3	1	11	7	5	1
		2	11	5	3	1
		3	11	3	10	1
12	1	1	12	17	19	15
		2	12	19	13	15
		3	12	13	9	15
	2	1	12	5	17	15
		2	12	3	5	15
		3	12	9	3	15
	3	1	12	7	5	3
		2	12	1	7	3
		3	12	9	1	3

Table 4. Cont.

Singular Point	Triangular Prism	Tetrahedron	Node 1	Node 2	Node 3	Node 4
14	1	1	14	17	15	5
		2	14	15	3	5
		3	14	3	2	5
	2	1	14	19	17	5
		2	14	7	19	5
		3	14	2	7	5
	3	1	14	13	19	7
		2	14	1	13	7
		3	14	2	1	7
16	1	1	16	19	17	7
		2	16	17	5	7
		3	16	5	4	7
	2	1	16	13	19	7
		2	16	1	13	7
		3	16	4	1	7
	3	1	16	15	13	1
		2	16	3	15	1
		3	16	4	3	1
18	1	1	18	17	15	3
		2	18	5	17	3
		3	18	6	5	3
	2	1	18	15	13	3
		2	18	13	1	3
		3	18	1	6	3
	3	1	18	13	19	1
		2	18	19	7	1
		3	18	7	6	1
20	1	1	20	15	13	3
		2	20	13	1	3
		3	20	1	8	3
	2	1	20	17	15	3
		2	20	5	17	3
		3	20	8	5	3
	3	1	20	19	17	5
		2	20	7	19	5
		3	20	8	7	5

3.1.4. Numerical Results

In the VIEM, the displacements and stresses inside the cubic inhomogeneity are first calculated using the models in Figure 4. We calculate the displacements and stresses outside the cubic inhomogeneity using Equation (2), by adding standard finite elements in appropriate locations.

Figure 8 shows typical VIEM models for the single cubic inhomogeneity ($-4 \text{ mm} \leq x, XX \leq 4 \text{ mm}$) (between two green lines) including the outside of the cubic inhomogeneity ($-8 \text{ mm} \leq x \leq -4 \text{ mm}$ and $4 \text{ mm} \leq x \leq 8 \text{ mm}$). Since $x \neq \xi$ outside the inhomogeneity, singularities do not exist while calculating the displacements and stresses outside the inhomogeneity in the VIEM. Therefore, the displacement and stress fields inside and outside the inhomogeneities can be solved without difficulty.

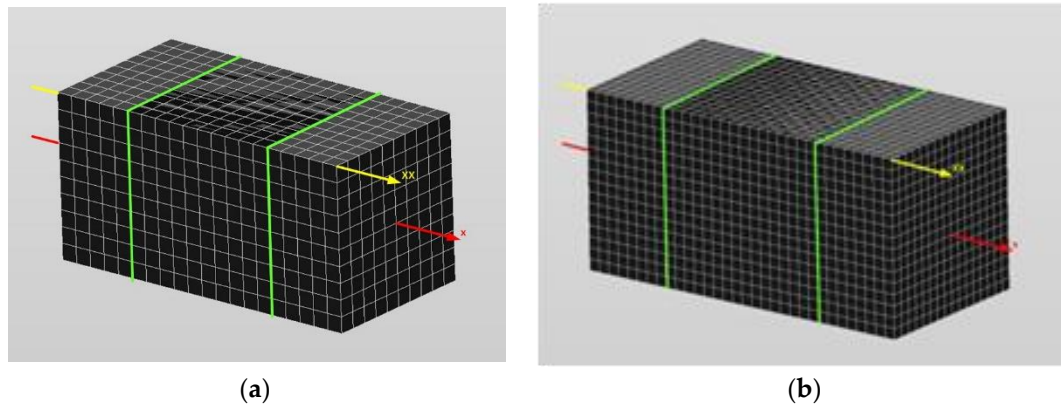


Figure 8. A typical single cubic model ($-4 \text{ mm} \leq x, XX \leq 4 \text{ mm}$) (between two green lines) including the outside of the cube ($-8 \text{ mm} \leq x \leq -4 \text{ mm}$ and $4 \text{ mm} \leq x \leq 8 \text{ mm}$) in the VIEM. (a) A single cubic model ($-4 \text{ mm} \leq x, XX \leq 4 \text{ mm}$) with 1000 elements (Model_10 \times 10 \times 10) (between two green lines) including the outside of the cube ($-8 \text{ mm} \leq x \leq -4 \text{ mm}$ and $4 \text{ mm} \leq x \leq 8 \text{ mm}$). 1000 elements are used for the discretization of the outside of the cube; (b) a single cubic model ($-4 \text{ mm} \leq x, XX \leq 4 \text{ mm}$) with 4096 elements (Model_16 \times 16 \times 16) (between two green lines) including the outside of the cube ($-8 \text{ mm} \leq x \leq -4 \text{ mm}$ and $4 \text{ mm} \leq x \leq 8 \text{ mm}$). 4096 elements are used for the discretization of the outside of the cube.

Figure 9 shows normalized tensile stress component ($\sigma_{xx}/\sigma_{xx}^0$) along the x-axis and the XX-axis ($-8 \text{ mm} \leq x, XX \leq 8 \text{ mm}$) for Model_8 \times 8 \times 8 (512 elements), Model_10 \times 10 \times 10 (1000 elements), Model_14 \times 14 \times 14 (2744 elements) and Model_16 \times 16 \times 16 (4096 elements) under uniform remote tensile loading for the isotropic cubic inhomogeneity. The remote applied load was assumed to be $\sigma_{xx}^0 = 143.1 \text{ GPa}$.

Standard 20-node quadratic hexahedral elements in Figure 6 were used in the VIEM models. In the Model_nxn, the symbol n represents the number of line segments split in each side of a cube. A cubic inhomogeneity ($-4 \text{ mm} \leq x, y, z \leq 4 \text{ mm}$) is divided into n^3 hexahedral elements in the Model_nxn. For example, in the Model_14 \times 14 \times 14, a cubic inhomogeneity ($-4 \text{ mm} \leq x, y, z \leq 4 \text{ mm}$) is divided into 2744 ($=14^3$) elements.

Figure 9a shows the normalized tensile stress component ($\sigma_{xx}/\sigma_{xx}^0$) along the x-axis inside the isotropic cubic inhomogeneity ($-4 \text{ mm} \leq x \leq 4 \text{ mm}$) and outside the isotropic cubic inhomogeneity ($-8 \text{ mm} \leq x \leq -4 \text{ mm}$ and $4 \text{ mm} \leq x \leq 8 \text{ mm}$), respectively. Figure 9b shows the normalized tensile stress component ($\sigma_{xx}/\sigma_{xx}^0$) along the XX-axis inside the isotropic cubic inhomogeneity ($-4 \text{ mm} \leq XX \leq 4 \text{ mm}$) and outside the isotropic cubic inhomogeneity ($-8 \text{ mm} \leq XX \leq -4 \text{ mm}$ and $4 \text{ mm} \leq XX \leq 8 \text{ mm}$), respectively. The results using the VIEM for the different models converged very well within this range of hexahedral elements.

Figures 10–12 show the normalized tensile stress component ($\sigma_{xx}/\sigma_{xx}^0$) along the x-axis and the XX-axis ($-8 \text{ mm} \leq x, XX \leq 8 \text{ mm}$) for Model_8 \times 8 \times 8, Model_10 \times 10 \times 10, Model_14 \times 14 \times 14 and Model_16 \times 16 \times 16 under uniform remote tensile loading for the three different orthotropic inhomogeneities (mat_01, mat_02 and mat_03), respectively. The remote applied load was assumed to be $\sigma_{xx}^0 = 143.1 \text{ GPa}$.

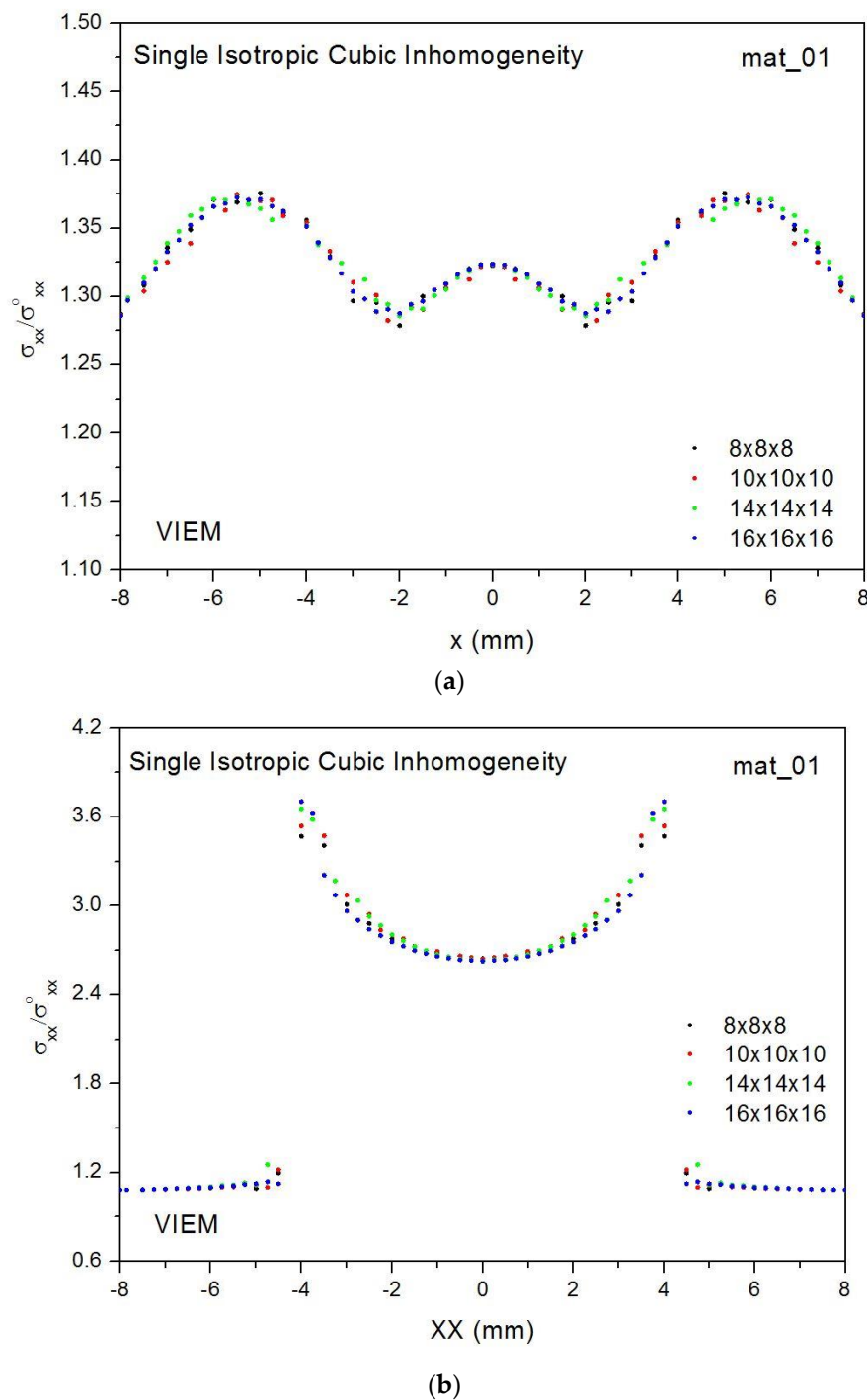


Figure 9. Numerical results using the volume integral equation method (VIEM) for the normalized tensile stress component ($\sigma_{xx}/\sigma_{xx}^0$) along the x -axis and the XX -axis ($-8 \text{ mm} \leq x, XX \leq 8 \text{ mm}$) for Model $8 \times 8 \times 8$, Model $10 \times 10 \times 10$, Model $14 \times 14 \times 14$ and Model $16 \times 16 \times 16$ under uniform remote tensile loading. (a) x -axis; (b) XX -axis.

Figure 10a shows the normalized tensile stress component ($\sigma_{xx}/\sigma_{xx}^0$) along the x -axis inside the orthotropic cubic inhomogeneity #1 (mat_02 in Table 2) ($-4 \text{ mm} \leq x \leq 4 \text{ mm}$) and outside the cubic inhomogeneity ($-8 \text{ mm} \leq x \leq -4 \text{ mm}$ and $4 \text{ mm} \leq x \leq 8 \text{ mm}$), respectively. Figure 10b shows the normalized tensile stress component ($\sigma_{xx}/\sigma_{xx}^0$) along the XX -axis inside the orthotropic cubic inhomogeneity #1 ($-4 \text{ mm} \leq XX \leq 4 \text{ mm}$) and outside the cubic inhomogeneity ($-8 \text{ mm} \leq XX \leq -4 \text{ mm}$ and $4 \text{ mm} \leq XX \leq 8 \text{ mm}$), respectively.

and $4 \text{ mm} \leq x \leq 8 \text{ mm}$), respectively. The VIEM solutions using the different models converged very well within this range of hexahedral elements.

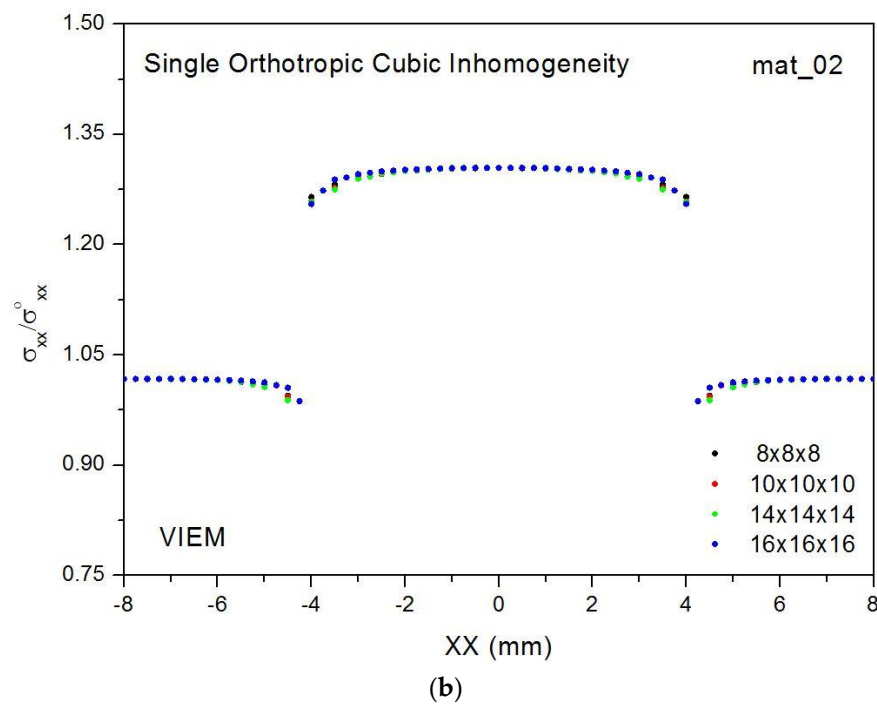
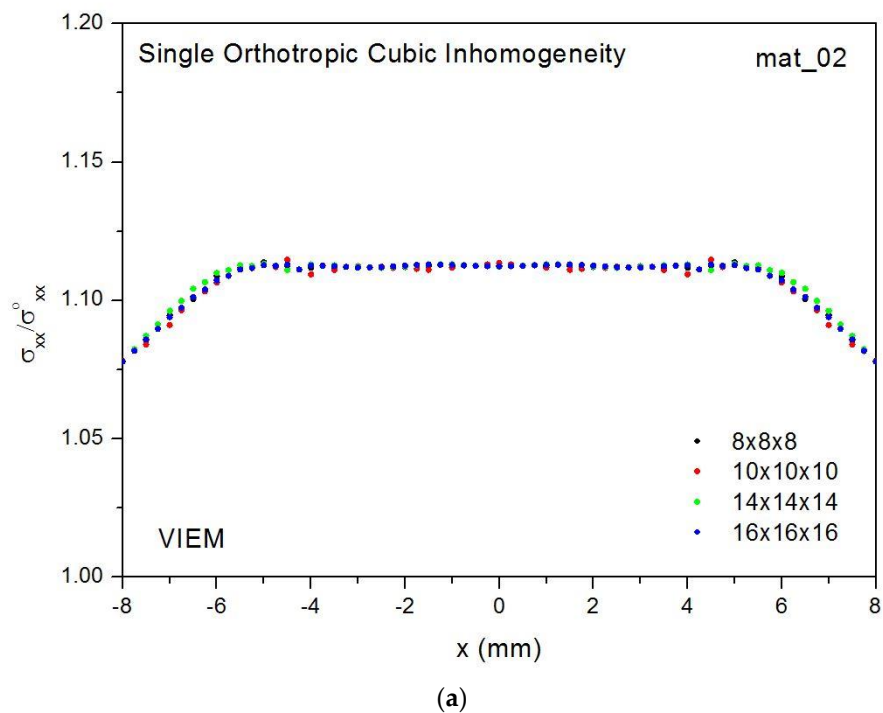


Figure 10. Numerical results using the volume integral equation method (VIEM) for the normalized tensile stress component ($\sigma_{xx}/\sigma_{xx}^0$) along the x-axis and the XX-axis ($-8 \text{ mm} \leq x, XX \leq 8 \text{ mm}$) for Model $8 \times 8 \times 8$, Model $10 \times 10 \times 10$, Model $14 \times 14 \times 14$ and Model $16 \times 16 \times 16$ under uniform remote tensile loading. (a) x-axis; (b) XX-axis.

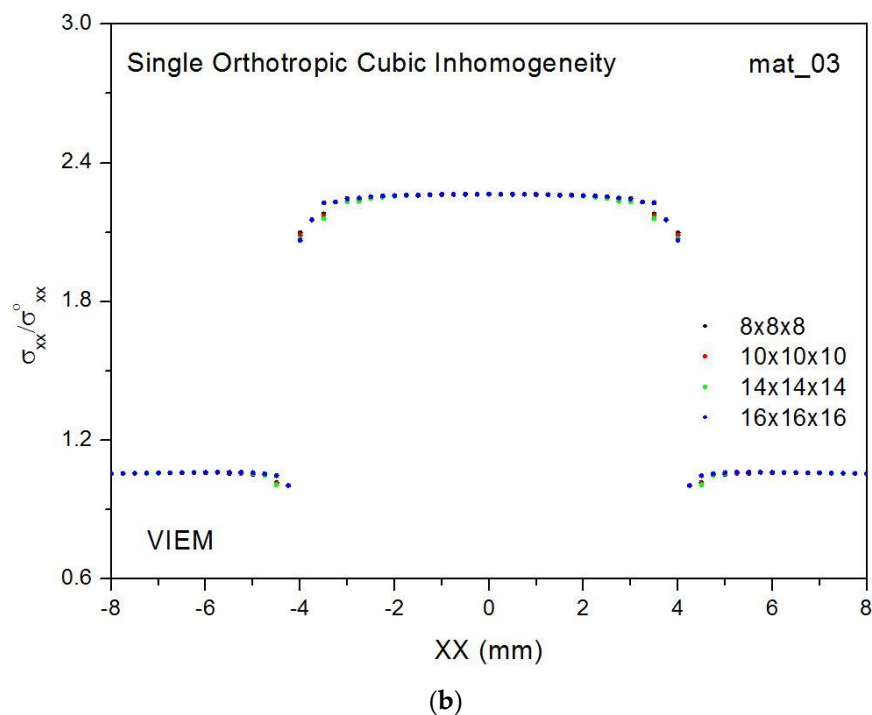
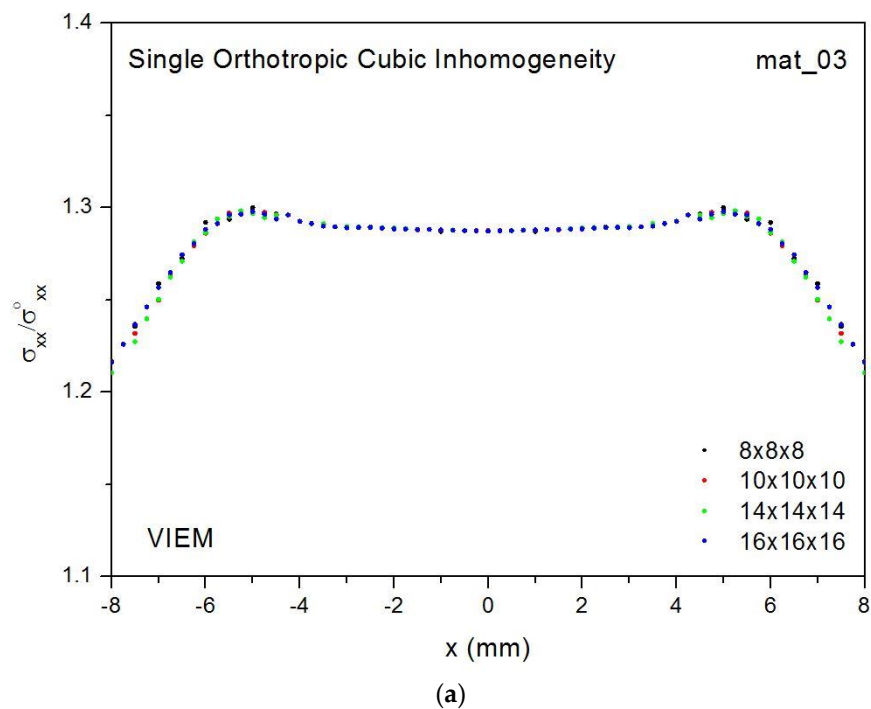


Figure 11. Numerical results using the volume integral equation method (VIEM) for the normalized tensile stress component ($\sigma_{xx}/\sigma_{xx}^0$) along the x-axis and the XX-axis ($-8 \text{ mm} \leq x, XX \leq 8 \text{ mm}$) for Model_8 \times 8 \times 8, Model_10 \times 10 \times 10, Model_14 \times 14 \times 14 and Model_16 \times 16 \times 16 under uniform remote tensile loading. (a) x-axis; (b) XX-axis.

Figures 11a and 12a show the same as Figure 10a for the orthotropic cubic inhomogeneity #2 and #3 (mat_03 and mat_04 in Table 2) ($-8 \text{ mm} \leq x \leq 8 \text{ mm}$), respectively. Figures 11b and 12b show the same as Figure 10b for the orthotropic cubic inhomogeneity #2 and #3 ($-8 \text{ mm} \leq XX \leq 8 \text{ mm}$), respectively. The results using the VIEM for the different models converged very well within this range of hexahedral elements.

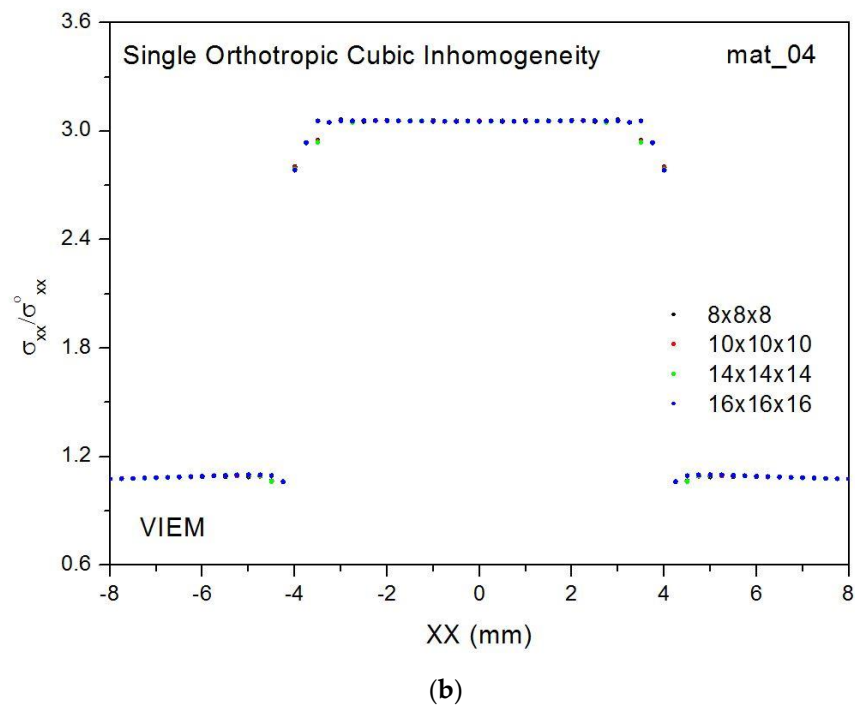
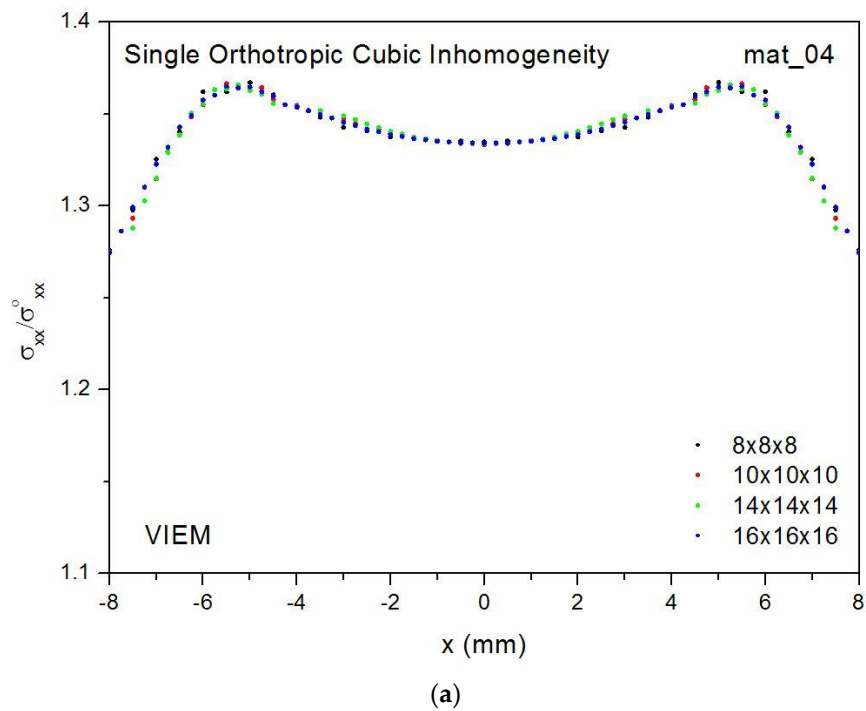


Figure 12. Numerical results using the volume integral equation method (VIEM) for the normalized tensile stress component ($\sigma_{xx}/\sigma_{xx}^0$) along the x-axis and the XX-axis ($-8 \text{ mm} \leq x, XX \leq 8 \text{ mm}$) for Model_8 \times 8 \times 8, Model_10 \times 10 \times 10, Model_14 \times 14 \times 14 and Model_16 \times 16 \times 16 under uniform remote tensile loading. (a) x-axis; (b) XX-axis.

The normalized tensile stress component ($\sigma_{xx}/\sigma_{xx}^0$) for the isotropic cubic inhomogeneity in Figure 9 appears to be considerably different from those of the orthotropic cubic inhomogeneities in Figures 10–12.

3.2. A single Spherical Inhomogeneity Problem

3.2.1. A Single Isotropic Spherical Inhomogeneity

In order to examine the accuracy of the numerical results using the VIEM, the numerical results using the VIEM for a single isotropic spherical inhomogeneity were first compared to the analytical solutions [21]. We considered a single isotropic spherical inhomogeneity with a radius of 7 mm in an unbounded isotropic matrix subject to uniform remote tensile loading, σ_{xx}^0 , as shown in Figure 13 (also see Figure 2b). In Figure 13, standard 20-node quadratic hexahedral elements in Figure 6 were used in the discretization [17]. The number of hexahedral elements was 4320. In order to investigate the accuracy of the hexahedral elements, only hexahedral elements without tetrahedral elements were used in Figure 13. The elastic properties of the isotropic matrix and the isotropic inhomogeneity for the calculations are given in Table 5.

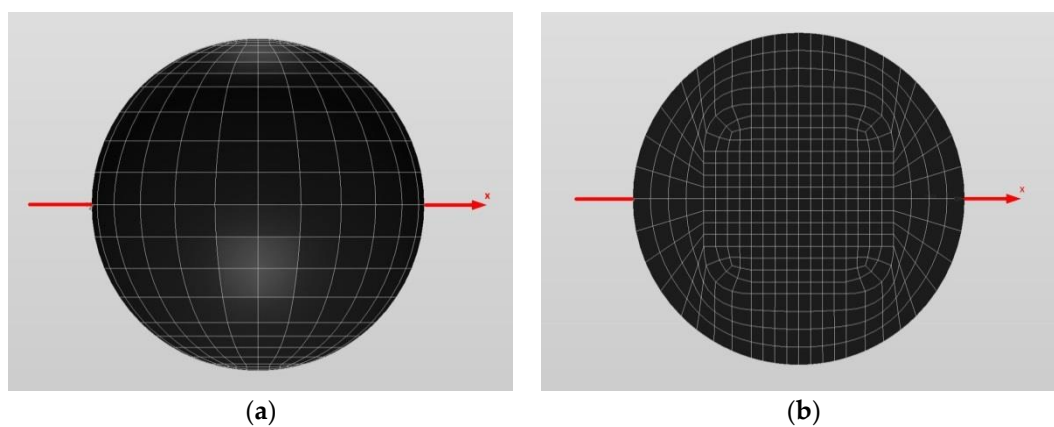


Figure 13. A typical discretized spherical model in the volume integral equation method (VIEM). (a) A spherical model; (b) an inside view of a spherical model.

Table 5. Material properties of the isotropic matrix and the isotropic spherical inhomogeneity.

	Isotropic Matrix (mat_05)	Isotropic Inhomogeneity (mat_05)	Isotropic Matrix (mat_06)	Isotropic Inhomogeneity (mat_06)
λ [GPa]	75.0	150.0	75.0	375.0
μ [GPa]	37.5	75.0	37.5	187.5

Figure 14 shows a comparison between the numerical results using the volume integral equation method (VIEM) and the analytical solutions [21] for the normalized tensile stress component ($\sigma_{xx}/\sigma_{xx}^0$) along the x-axis inside the isotropic spherical inhomogeneities with a radius of 7 mm under uniform remote tensile loading. The remote applied load was assumed to be $\sigma_{xx}^0 = 150.0$ GPa.

It should be noted that the normalized tensile stress component ($\sigma_{xx}/\sigma_{xx}^0$) inside the isotropic spherical inhomogeneities was found to be constant [21,22].

Eshelby [22] solved the inhomogeneity problem of an ellipsoidal inclusion using the equivalent inclusion method. The stresses inside the inclusion are determined by:

$$\sigma_{ij}^i = c_{ijkl}^{(2)}(\varepsilon_{kl}^c - \varepsilon_{kl}^*) = c_{ijkl}^{(2)}(S_{klpq}\varepsilon_{pq}^* - \varepsilon_{kl}^*) \quad (16)$$

where $c_{ijkl}^{(2)}$ represents the fourth-order elasticity tensors of the matrix and $\varepsilon_{kl}^{(c)}$ stands for the constraint strain ($\varepsilon_{kl}^{(c)} = S_{klpq}\varepsilon_{pq}^*$). ε_{kl}^* represents the eigenstrain of the equivalent inclusion and S_{klpq} represents Eshelby's fourth-order tensor. It should be noted that the Eshelby's tensor satisfies minor symmetries, $S_{ijkl} = S_{jikl} = S_{ijlk}$.

In order to obtain the analytical solution, we used Equations (5) and (6) in Shibata and Ono [21] and the expressions in Equation (17):

$$\begin{aligned} S_{1111} = S_{2222} = S_{3333} &= \frac{(7-5\nu)}{15(1-\nu)}, \\ S_{1122} = S_{2233} = S_{3311} = S_{1133} = S_{3322} = S_{2211} &= \frac{(5\nu-1)}{15(1-\nu)}, \\ S_{1212} = S_{2323} = S_{3131} &= \frac{(4-5\nu)}{15(1-\nu)}. \end{aligned} \quad (17)$$

In Equation (17), ν is Poisson's ratio for the matrix material.

For the isotropic spherical inhomogeneity (mat_05), the analytical solution was 1.309091. For the isotropic spherical inhomogeneity (mat_06), the analytical solution was 1.617336. An excellent agreement was found between the analytical and numerical solutions using the VIEM for both cases considered. Figure 14 shows that the percentage differences for the two sets of results are less than 1% in both cases.

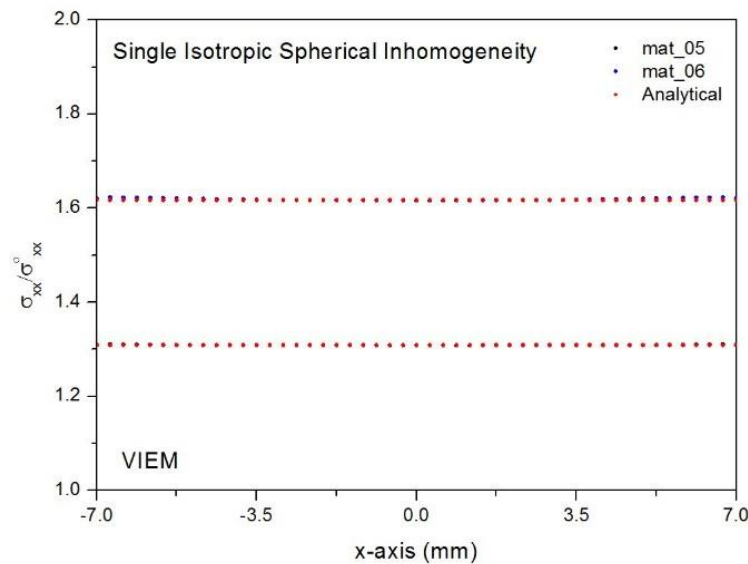


Figure 14. Comparison of the numerical results using the volume integral equation method (VIEM) and the analytical solutions for the normalized tensile stress component ($\sigma_{xx}/\sigma^0_{xx}$) along the x-axis inside the isotropic spherical inclusions with a radius of 7 mm under uniform remote tensile loading.

3.2.2. A Single Orthotropic Spherical Inhomogeneity

We consider a single orthotropic spherical inhomogeneity in an unbounded isotropic matrix under uniform remote tensile loading, σ_{xx}^0 , as shown in Figure 13 (also see Figure 2b). The elastic properties of the isotropic matrix and orthotropic inhomogeneities used in these calculations are given in Table 2.

Figure 15 shows the numerical results using the volume integral equation method (VIEM) for the normalized tensile stress component ($\sigma_{xx}/\sigma^0_{xx}$) along the x-axis inside the orthotropic spherical inhomogeneities (the orthotropic inhomogeneity #1 and #2; mat_02 and mat_03 in Table 2) with a radius of 7 mm under uniform remote tensile loading. The remote applied load was assumed to be $\sigma^0_{xx} = 143.1$ GPa. It should be noted that the normalized tensile stress component ($\sigma_{xx}/\sigma^0_{xx}$) inside the orthotropic spherical inhomogeneities was found to be constant [23].

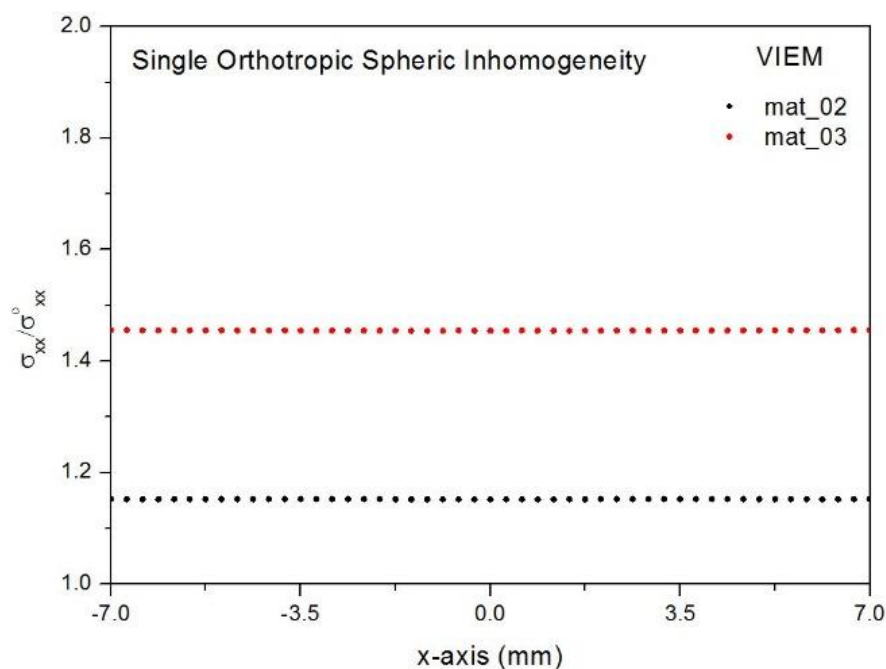


Figure 15. Numerical results using the volume integral equation method (VIEM) for the normalized tensile stress component ($\sigma_{xx}/\sigma^0_{xx}$) along the x-axis inside the orthotropic spherical inclusions with a radius of 7 mm under uniform remote tensile loading.

4. Conclusions

The volume integral equation method was applied to a class of three-dimensional elastostatic inhomogeneity problems. First, we introduced the details of the numerical treatment, especially the evaluation of singular integrals, for solving three-dimensional problems using the VIEM. We considered a single isotropic or orthotropic cubic inhomogeneity ($-4 \text{ mm} \leq x, y, z \leq 4 \text{ mm}$) in the unbounded isotropic matrix under uniform remote tensile loading.

It was determined that the VIEM solutions, using the different models, converged very well for all cases. Next, we considered a single isotropic/orthotropic spherical inhomogeneity in an unbounded isotropic matrix under uniform remote tensile loading. An excellent agreement was found between the analytical and numerical solutions using the VIEM for single isotropic spherical inhomogeneity problems. The normalized tensile stress component ($\sigma_{xx}/\sigma^0_{xx}$) inside the spherical inhomogeneities was also found to be constant for the single orthotropic spherical inhomogeneity problems.

The major merit of the volume integral equation method (VIEM), compared to the finite element method (FEM), is that it needs discretization of the inhomogeneities only as opposed to discretization of the whole domain. In elastodynamic problems, involving multiple anisotropic inhomogeneities, numerical treatment of the BIEM is very difficult to achieve, since closed-form analytical expressions of the elastodynamic Green's functions in anisotropic media are currently not available. By contrast, the VIEM does not require the use of Green's functions for anisotropic inhomogeneities. Since the VIEM is designed to use standard finite elements, it is simpler and more advantageous for dealing with multiple non-smooth anisotropic inhomogeneities. Thus, the VIEM is now generally more applicable and executable than the boundary element or finite element methods. Moreover, the volume integral equation method (VIEM) can be used to compute critical values of practical interest in realistic models of composites with strong anisotropic inhomogeneities of arbitrary shapes.

Author Contributions: Conceptualization, J.L.; VIEM Analysis, J.L.; Investigation, J.L. and M.H.; Validation, M.H. and J.L.; Writing-original draft, J.L. All authors have read and agreed to the published version of the manuscript.

Funding: This research was supported by the Ministry of Trade, Industry and Energy (MOTIE), KOREA, through the Education Program for Creative and Industrial Convergence (No. N0000717) and 2019 Hongik University Research Fund. This work was also supported by the National Supercomputing Center with supercomputing resources including technical support (No. KSC-2020-CRE-0107) and the National Research Foundation of Korea (NRF) grant funded by the Korea government (MSIT) (No. 2019R1H1A2039647).

Acknowledgments: The authors would like to thank all reviewers and journal editors for their constructive and motivating comments. The authors also thank Jason P. Buschman at Hongik University (Sejong Campus) for his thorough proofreading of the revised manuscript.

Conflicts of Interest: The authors declare no conflict of interest.

References

1. Bose, S.K.; Mal, A.K. Elastic waves in a fiber-reinforced composite. *J. Mech. Phys. Solids* **1974**, *22*, 217–229. [\[CrossRef\]](#)
2. Maslov, B.P. Stress concentration in an isotropic matrix bonded by anisotropic fibers. *Sov. Appl. Mech.* **1987**, *23*, 963–969. [\[CrossRef\]](#)
3. Yang, R.B.; Mal, A.K. The effective transverse moduli of a composite with degraded fiber-matrix interfaces. *Int. J. Eng. Sci.* **1995**, *33*, 1623–1632. [\[CrossRef\]](#)
4. Lee, J.K.; Mal, A.K. A volume integral equation technique for multiple inclusion and crack interaction problems. *J. Appl. Mech.* **1997**, *64*, 23–31. [\[CrossRef\]](#)
5. Lee, J.K.; Mal, A.K. A volume integral equation technique for multiple scattering problems in elastodynamics. *Appl. Math. Comput.* **1995**, *67*, 135–159. [\[CrossRef\]](#)
6. Nimmer, R.P.; Bankert, R.J.; Russel, E.S.; Smith, G.A.; Wright, P.K. Micromechanical modeling of fiber/matrix interface effects in transversely loaded SiC/Ti-6-4 metal matrix composites. *J. Compos. Tech. Res.* **1991**, *13*, 3–13.
7. Lee, J.; Mal, A. Characterization of matrix damage in metal matrix composites under transverse loads. *Comput. Mech.* **1998**, *21*, 339–346. [\[CrossRef\]](#)
8. Aghdam, M.M.; Falahatgar, S.R. Micromechanical modeling of interface damage of metal matrix composites subjected to transverse loading. *Compos. Struct.* **2004**, *66*, 415–420. [\[CrossRef\]](#)
9. Mal, A.K.; Knopoff, L. Elastic wave velocities in two component systems. *J. Inst. Math. Appl.* **1967**, *3*, 376–387. [\[CrossRef\]](#)
10. Lee, J.K.; Lee, H.C.; Jeong, H.G. Multiple scattering using parallel volume integral equation method: Interaction of SH waves with multiple multilayered anisotropic elliptical inclusions. *Math. Probl. Eng.* **2015**. [\[CrossRef\]](#)
11. Lee, J.K.; Lee, H.M.; Mal, A. A mixed volume and boundary integral equation technique for elastic wave field calculations in heterogeneous materials. *Wave Motion* **2004**, *39*, 1–19. [\[CrossRef\]](#)
12. Buryachenko, V.A. *Micromechanics of Heterogeneous Materials*; Springer: New York, NY, USA, 2007.
13. *Advances in Computers and Information in Engineering Research*; Michopoulos, J.G.; Rosen, D.W.; Paredis, C.J.; Vance, J.M. (Eds.) ASME Press: New York, NY, USA, 2020; Volume 2, in press.
14. Lee, J.K.; Oh, S.M.; Mal, A. Calculation of interfacial stresses in composites containing elliptical inclusions of various types. *Eur. J. Mech. A Solid.* **2014**, *44*, 17–40. [\[CrossRef\]](#)
15. Buryachenko, V.A.; Bechel, V.T. A series solution of the volume integral equation for multiple-inclusion interaction problems. *Compos. Sci. Technol.* **2000**, *60*, 2465–2469. [\[CrossRef\]](#)
16. Buryachenko, V.A. Solution of general integral equations of micromechanics of heterogeneous materials. *Int. J. Solids Struct.* **2014**, *51*, 3823–3843. [\[CrossRef\]](#)
17. *PATRAN User's Manual*, version 2008 r2; MSC Software: Newport Beach, CA, USA, 2008.
18. Banerjee, P.K. *The Boundary Element Methods in Engineering*; McGraw-Hill: London, UK, 1993.
19. Pao, Y.-H.; Varatharajulu, V. Huygens' principle, radiation conditions, and integral formulas for the scattering of elastic waves. *J. Acoust. Soc. Am.* **1976**, *59*, 1361–1369. [\[CrossRef\]](#)
20. Li, H.B.; Han, G.M.; Mang, H.A. A new method for evaluating singular integrals in stress analysis of solids by the direct boundary element method. *Int. J. Numer. Methods Eng.* **1985**, *21*, 2071–2098. [\[CrossRef\]](#)
21. Shibata, M.; Ono, K. Stress concentration due to a prolate spheroidal inclusion. *J. Compos. Mater.* **1978**, *12*, 132–138. [\[CrossRef\]](#)

22. Eshelby, J.D. The determination of the elastic field of an ellipsoidal inclusion and related problems. *Proc. Royal Soc. A* **1957**, *241*, 376–396.
23. Ma, H. Solutions of Eshelby-Type Inclusion Problems and a Related Homogenization Method Based on a Simplified Strain Gradient Elasticity Theory. Ph.D. Thesis, Department of Mechanical Engineering, Texas A&M University, College Station, TX, USA, 2010.

Publisher’s Note: MDPI stays neutral with regard to jurisdictional claims in published maps and institutional affiliations.



© 2020 by the authors. Licensee MDPI, Basel, Switzerland. This article is an open access article distributed under the terms and conditions of the Creative Commons Attribution (CC BY) license (<http://creativecommons.org/licenses/by/4.0/>).